AIAA JOURNAL
Vol. 34, No. 4, April 1996

Comparison of Eddy Viscosity–Transport Turbulence Models for Three-Dimensional, Shock-Separated Flowfields

Jack R. Edwards*
North Carolina State University, Raleigh, North Carolina 27695
and
Suresh Chandra†
North Carolina A&T State University, Greensboro, North Carolina 27411

An evaluation of four one-equation eddy viscosity–transport turbulence closure models as applied to three-dimensional shock wave/boundary-layer interactions is presented herein. Comparisons of two versions of the Baldwin–Barth model, an approach of Edwards and McRae, and a modified form of the Spalart–Allmaras model are presented for two test cases, one involving Mach 8 flow over a flat plate/sharp fin apparatus and the other involving Mach 3 flow over a cylinder–offset-cone geometry. Strengths and weaknesses of the one-equation approaches are highlighted through direct comparison with experimental data, and the effect of grid refinement is examined.

I. Introduction

SEVERAL works[1–6] have advocated the eddy viscosity–transport approach as a means of closing the Reynolds-averaged Navier–Stokes system for complex, wall-bounded flows. The original concept of a single transport equation governing directly the development of the eddy viscosity field was proposed by Nee and Kovasznay[1] in the late 1960s. After lying dormant in this country for 20 years, the idea was rediscovered by Baldwin and Barth,[2] who developed a near-wall calibration procedure and an efficient strategy for advancing the solution of the eddy viscosity equation. Since the publication of Ref. 2, there has been steady progress in the development of eddy viscosity–transport methods in the United States. Spalart and Allmaras[3] at Boeing, Durbin and Yang[4] at the Center for Turbulance Research, and Edwards and McRae[5] and Edwards and Chandra[6] at North Carolina State University and North Carolina A&T State University have all derived variations on the basic theme, each with its own degree of complexity and applicability. Independent testing of some of these approaches has been performed by Menter[7] for low Mach number adverse pressure gradient flows, by Kandula and Buning[8] for exhaust jet flowfields, by Birch[9] for mixing layers, and by Goldberg and Ramakrishnan[10] for a wide variety of flows. None of the flows considered in the tests were three dimensional, and except for a few computations by Goldberg and Ramakrishnan,[10] all were at either subsonic or transonic conditions.

Basic comparisons among several of the approaches for two-dimensional supersonic/hypersonic shock/boundary-layer interactions have been presented in Ref. 6. Several general deficiencies of the various eddy viscosity–transport methodologies were delineated, with the most notable being a failure to predict the proper recovery of a turbulent boundary layer following a strong disturbance. It was noted, however, that the baseline models (Baldwin–Barth, Spalart–Allmaras, and Edwards–McRae) were generally able to predict both the upstream extent of axial separation and the wakelike velocity distribution above the backflow region quite well.

In this paper, we attempt to ascertain the degree of accuracy and predictive capability offered by four eddy viscosity–transport approaches for three-dimensional flow situations involving shock wave/turbulent boundary-layer interaction. Two versions of the Baldwin–Barth model are considered, one very similar to the original presentation[6] and the other a pointwise modification of the original.[10] The Edwards–McRae model and a modified version of the Spalart–Allmaras model are also included in the comparative study. Two recently obtained experimental databases are considered as a means toward achieving our goals. The first database corresponds to an experiment by Kussoy and Horstman[11] and involves Mach 8 flow over a flat plate/sharp fin geometry. The second database corresponds to an experiment by Wideman et al.[12] and involves Mach 3 flow over a cylinder–offset-cone configuration. Comparisons with the experimental data, both in regard to surface measurements and to the postulated flowfield structure, will be used to delineate the relative strengths and weaknesses of the closure concepts for these flows. The effect of grid refinement on the obtained solutions and convergence rates will also be examined.

Presented as Paper 94-2275 at the AIAA 25th Fluid Dynamics Conference, Colorado Springs, CO, June 20–23, 1994; received Dec. 23, 1994; revision received June 5, 1995; accepted for publication June 5, 1995.

*Assistant Professor, Department of Mechanical and Aerospace Engineering, Campus Box 7910. Member AIAA.
†Research Professor, Department of Mechanical Engineering, McNair Hall. Member AIAA.

II. Governing Equations, Discretization Approach, and Numerical Method

The flowfields under consideration are assumed to be governed by the three-dimensional, compressible, Reynolds-averaged Navier–Stokes equations. Reynolds stress effects are incorporated by invoking the Boussinesq hypothesis, thus reducing the problem to the specification of an eddy viscosity and a turbulent Prandtl number (0.9 in this work). Compressibility effects are assumed to result solely from variations in the mean density.

A control volume discretization of the Navier–Stokes equation set is adopted, with a second-order MUSCL extension of the Wada–Liou[13] upwinding scheme used for the inviscid fluxes. The Wada–Liou approach is a hybrid flux-vector/flux-difference splitting technique that is capable of capturing shear layers without excess numerical diffusion. The viscous components of the Navier–Stokes set are central differenced to second-order accuracy.

The three-dimensional Reynolds-averaged Navier–Stokes set is solved using a recently developed upwind relaxation multigrid algorithm.[14] This approach, an extension of the nonlinear relaxation method described in Ref. 5, is capable of providing rapid convergence for three-dimensional, shock-separated flowfields. The one-equation models described next are solved in tandem with the mean flow equations. The discretization of the models follows that suggested by Baldwin and Barth,[2] and an implicit planar relaxation approach (performed only on the finest grid level) is used to advance the solution of the transport equations.

III. Turbulence Model Descriptions

In this section, the Edwards–McRae approach and two versions of the Baldwin–Barth model[6,10] are outlined in brief. A modified version of the Spalart–Allmaras model, incorporating an alternative calibration procedure for the viscous sublayer, is also described.

In terms of the transported quantity $F \equiv k^2/\epsilon$, the eddy viscosity field for the Baldwin–Barth variants and the Edwards–McRae model is defined as

$$\mu_t = \rho C_\mu F f_\mu \equiv \rho \nu_t \tag{1}$$

where C_μ is a constant and f_μ is a wall-damping function. The distribution of F is determined by the solution of

$$B_1 \frac{DF}{Dt} = \left(C_{\epsilon_2} f_2 - C_{\epsilon_1}\right)\sqrt{F\nu_t S} + \left(\nu + \frac{\nu_t}{\sigma_R}\right)\nabla^2 F - \frac{1}{\sigma_\epsilon}(\nabla \nu_t)\cdot \nabla F \tag{2}$$

for the Baldwin–Barth variants and

$$B_1 \frac{DF}{Dt} = B_2 f_2 \sqrt{F\nu_t S} + \frac{1}{\sigma_R}(\nu + \nu_t)\nabla^2 F - \frac{1}{\sigma_\epsilon}\frac{\nu_t F}{\hat{n}^2} \tag{3}$$

for the Edwards–McRae approach. In the preceding expressions, ν is the kinematic molecular viscosity, $\hat{n}$ is a representative distance from the wall (or walls), and

$$S = \left(\frac{\partial U_i}{\partial x_j} + \frac{\partial U_j}{\partial x_i}\right)\frac{\partial U_i}{\partial x_j} - \frac{2}{3}\left(\frac{\partial U_k}{\partial x_k}\right)^2$$

The wall-damping function f_μ is defined as

$$f_\mu = \left[1 - \exp\left(-\hat{n}^+/C_1^+\right)\right]\left[1 - \exp\left(-\hat{n}^+/C_2^+\right)\right] \tag{4}$$

for the Edwards–McRae model and the Baldwin–Barth variant of Ref. 6 and as

$$f_\mu = [1 - \exp(-A_\mu\sqrt{F/\nu})]/[1 - \exp(-A_\epsilon\sqrt{F/\nu})] \tag{5}$$

for the Baldwin–Barth variant of Goldberg and Ramakrishnan.[10] Forms for the wall-damping function f_2 are determined by considering the behavior of the equations in the near-wall region of a zero pressure gradient, flat plate boundary layer. In the interest of brevity, the reader is referred to Refs. 2, 6, and 10 for the actual expressions for f_2 and for values of the modeling constants. Multiple wall effects in the definition of $\hat{n}$ are accounted for by first measuring the distances from each wall to the point in question and then determining the minimum distance.

Both the Baldwin–Barth version presented in Ref. 6 and the Edwards–McRae model utilize an alternative definition of the wall coordinate $\hat{n}^+$,

$$\hat{n}^+ = \frac{[(C_\mu F/\kappa) + \beta U\hat{n}]}{\nu} \tag{6}$$

where β is a constant and U is the magnitude of the flow velocity vector $\boldsymbol{U}$. The second term in Eq. (6) allows some control over the numerical transition length provided by the models.[6] For zero pressure gradient boundary-layer flows, $F = \kappa U_\tau \hat{n}/C_\mu$ in the logarithmic region and below (κ is the von Kármán constant), and $\hat{n}^+$ reduces to its more conventional form $U_\tau \hat{n}/\nu$, where U_τ is the friction velocity. For other situations, the chosen form of $\hat{n}^+$ may differ from the more conventional definition, as the balances that lead to the linear representation for F in the near-wall region may be disrupted. The only difference between the Baldwin–Barth variant of Ref. 6 and the original presentation of Ref. 2 is the use of Eq. (6), which does not require an evaluation of a wall shear stress. As such, we will refer to this version as the Baldwin–Barth model throughout the remainder of the paper and will refer to the version of Ref. 10 as the G–R variant.

A modified version of the Spalart–Allmaras model is also considered in the comparative study. For this approach, the eddy viscosity field is defined as

$$\mu_t = \rho \tilde{\nu} f_{v1} \equiv \rho \nu_t \tag{7}$$

where the damping function f_{v1} is given by

$$f_{v1} = \lambda^3/\left(\lambda^3 + c_{v1}^3\right), \qquad \lambda \equiv \tilde{\nu}/\nu \tag{8}$$

The distribution of $\tilde{\nu}$ is determined by the solution of

$$\frac{D\tilde{\nu}}{Dt} = c_{b1}\tilde{S}\tilde{\nu} + \frac{1}{\sigma}\left\{\nabla\cdot[(\nu + \tilde{\nu})\nabla\tilde{\nu}] + c_{b2}(\nabla\tilde{\nu})^2\right\} - c_{w1} f_w(r)\left(\frac{\tilde{\nu}}{\hat{n}}\right)^2 \tag{9}$$

Differences between the modified Spalart–Allmaras model and the original version relate mainly to the modeled near-wall behavior of the strain-rate norm $\tilde{S}$. In the original version,[3]

$$\tilde{S} = S^{\frac{1}{2}} + \frac{\tilde{\nu}}{(\kappa\hat{n})^2} f_{v2}, \qquad f_{v2} = 1 - \frac{\lambda}{1 + \lambda f_{v1}} \tag{10}$$

The argument of the wall-blockage function f_w is defined using $\tilde{S}$,

$$r = \tilde{\nu}/(\kappa\hat{n})^2\tilde{S} \tag{11}$$

This form for $\tilde{S}$ ensures that the strain-rate norm maintains its logarithmic value ($U_\tau/\kappa\hat{n}$) all of the way to the wall. In our original implementation of the Spalart–Allmaras model,[6] the combination of the singular behavior of $\tilde{S}$ in the near-wall region, the lack of an exact linearization of $\tilde{S}$ (and f_w) in the implicit formulation of Eq. (9), and the large time steps allowed by the upwind relaxation flow solver produced oscillatory, limit-cycle convergence behavior in the Navier–Stokes residual norm after an initial period of rapid decrease. Such behavior made it difficult to judge the progress of the solution in any rigorous sense; flow properties such as skin friction and heat transfer had to be monitored instead.

A more stable way of accounting for the behavior of $\tilde{S}$ in the laminar sublayer can be derived by applying ideas from Refs. 2 and 6. The result is given by the following redefinitions:

$$\tilde{S} = S^{\frac{1}{2}}[(1/\lambda) + f_{v1}] \tag{12}$$

$$r = \frac{\tanh[\tilde{\nu}/(\kappa\hat{n})^2\tilde{S}]}{[\tanh(1.0)]} \tag{13}$$

The modified Spalart–Allmaras model allows smooth, rapid convergence while retaining the near-wall accuracy of the original formulation. Additional constants and functions used in both Spalart–Allmaras formulations can be found in Ref. 3.

A major difference between the Edwards–McRae and Spalart–Allmaras models and the Baldwin–Barth formulations is the inclusion, in the first two, of destruction terms dependent on a representative distance from a solid surface. These terms are generally important only in the logarithmic region and below; their influence decays rapidly in the outer part of the boundary layer. Nevertheless, their inclusion serves to disrupt the coordinate-invariance of the transport equations, and as a result, the Edwards–McRae and Spalart–Allmaras models may be more difficult to apply in extremely complex settings. In contrast, the Baldwin–Barth variants are very nearly coordinate invariant, with the G–R version being completely so. The other Baldwin–Barth variant displays a weak dependence on the wall distance, manifested through the wall-coordinate definition of Eq. (6). This dependence is needed only to induce the initial numerical transition; once enough eddy viscosity has been generated, the term is no longer needed. In the near-wall region, the diffusion term $-(1/\sigma_\epsilon)(\nabla\nu_t)\cdot\nabla F$ in Eq. (2) behaves similarly to the destruction terms in the Edwards–McRae and Spalart–Allmaras models. Away from the wall, however, the influence of the term does not vanish, and it acts to oppose the production-of-eddy viscosity term $(C_{\epsilon_2} f_2 - C_{\epsilon_1})\sqrt{(F\nu_t S)}$ in the outer layer.

IV. Results

Two recently obtained experimental databases involving three-dimensional shock/boundary-layer interaction are used to evaluate the performance of the eddy viscosity–transport approaches. The first database corresponds to an experiment by Kussoy and Horstman[11] and involves the Mach 8.2 interaction of a developing flat-plate turbulent boundary layer with the planar shock surface generated by a 15-deg fin placed perpendicular to the plate. The second database corresponds to a more recent experiment of

Table 1 Experiment parameters

	Kussoy–Horstman 15-deg fin	Wideman et al. cylinder–cone
Mach number	8.20	2.89
Re/m	5.32×10^6	1.7×10^7
T_∞, K	76.89	105.0
T_{wall}/T_∞	3.90	adiabatic
Inflow δ, cm	3.7	1.10
Inflow θ, cm	9.4×10^{-2}	N/A
Inflow C_f	1.0×10^{-3}	1.44×10^{-3}
Inflow q_w, W/cm^2	1.04	N/A

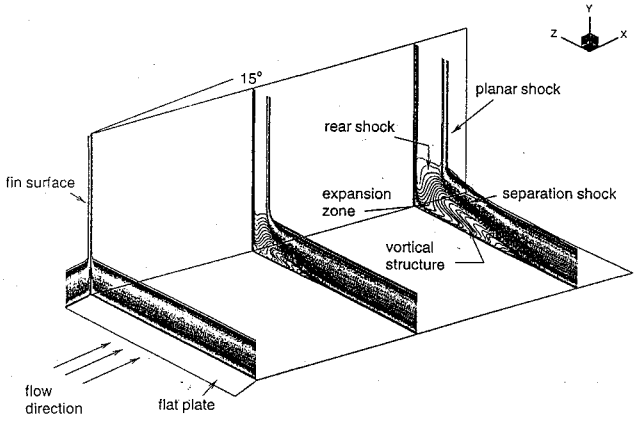

Fig. 1 Mach number contours; Ref. 11 15-deg fin.

Wideman et al.[12] and involves Mach 2.89 flow over a cylinder–20-deg cone configuration. Pertinent freestream and inflow boundary-layer properties for both interactions are summarized in Table 1. For the Kussoy–Horstman case, the apex of the fin was located 176 cm downstream of the flat plate leading edge, and the boundary layer was surveyed (in the absence of the fin) at a location 187 cm downstream of the leading edge. In the Wideman et al. experiment, the inflow boundary layer was surveyed at a location 2 cm upstream of the cylinder–cone juncture at the top of the apparatus. The inflow profiles for the computations were determined by integrating the two-dimensional (axisymmetric) Reynolds-averaged Navier–Stokes equations over a flat plate (cylinder) until the conditions in the preceding table were matched to sufficient accuracy.

A. Kussoy–Horstman Sharp Fin

The baseline grid used for the Kussoy–Horstman computations consists of 97 points in the streamwise (X) direction, 65 points normal to the flat plate (Y), and 89 points normal to the fin surface (Z). A finer grid consisting of $113 \times 97 \times 113$ nodes is also used to assess the grid dependence of the obtained solutions and convergence rates. The degree of clustering in the Y and Z directions is such that a minimum $\hat{n}^+$ of 1.0 or smaller is maintained in the equilibrium regions upstream of the interaction.

Representative Mach number contours for the Kussoy–Horstman geometry are shown in Fig. 1 ($97 \times 65 \times 89$ grid, Edwards–McRae model). The fin-generated oblique shock separates the flat-plate viscous layer, producing a vortical structure that grows in a nearly conical fashion for a short distance away from the fin leading edge. Boundary-layer displacement effects result in the formation of separation and rear shock surfaces. An expansion fan caused by the curving of the external flow around the thickened viscous layer is also observed in the region between the fin and the planar shock surface.

In Fig. 2, crossflow surface pressure distributions corresponding to each of the models are compared with the experimental data at $X = 18.2$ cm (measured relative to the fin apex). The lateral extent of the crossflow vortical structure and the magnitude of the separation-shock pressure rise are predicted well by the Baldwin–Barth, Spalart–Allmaras, and Edwards–McRae computations. The pointwise G–R computation predicts a larger extent of crossflow separation but predicts the peak pressure near the fin ($Z = 0$) rather well. More significant differences among the model predictions are

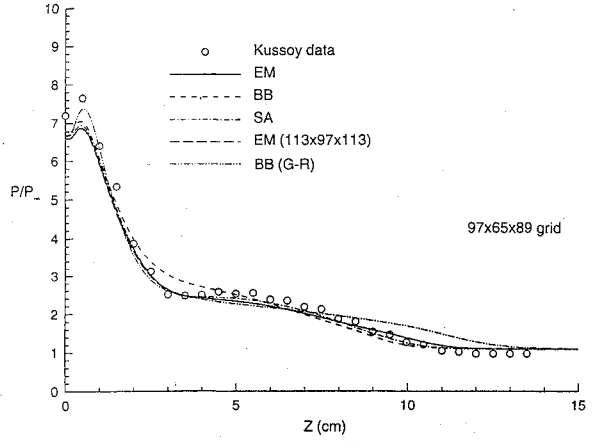

Fig. 2 Plate pressure; Ref. 11 15-deg fin, X = 18.2 cm: Edwards–McRae EM, Baldwin–Barth BB, Spalart–Allmaras SA, and Goldberg–Ramakrishnan BB (G–R).

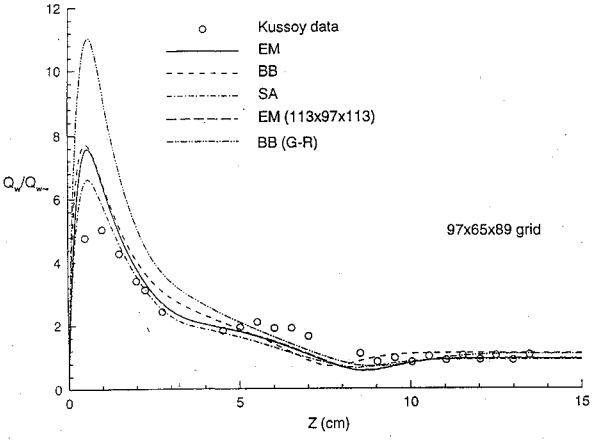

Fig. 3 Plate heat transfer; Ref. 11 15-deg fin, X = 16.45 cm.

evidenced in Fig. 3, a plot of the normalized lateral heat transfer at $X = 16.45$ cm. The rise in heat transfer near the fin surface, a consequence of the movement of the high-temperature external flow behind the shock to the surface via vortex action, is overpredicted by all approaches. A second peak in heat transfer at $Z \approx 6$ cm, a possible result of a secondary separation, is not captured by any of the computations. In general, the Spalart–Allmaras solution displays the best agreement with the measured heat transfer level near the fin, whereas the Edwards–McRae solution more accurately captures the lateral extent of the heat transfer rise. The results from the two Baldwin–Barth variants differ significantly, with the G–R solution overestimating both the experimental peak heat transfer and the Baldwin–Barth prediction by a large margin.

Such large deviations in the solutions provided by the Baldwin–Barth and G–R models can be traced to the behavior of the damping functions f_μ [Eqs. (4) and (5)] with changing viscosity ratio F/ν. Using the constants given in Refs. 2 and 10, it can be shown that the damping function of Eq. (5) approaches its limiting value of unity (increasing F/ν) and its limiting value of zero (decreasing F/ν) much more slowly than the damping function of Eq. (4). One result is that the damping function of Eq. (5) lowers, unnecessarily, the level of eddy viscosity in the outer part of the viscous layer. The computed boundary layers are less energetic and, thus, are more prone to flow reversal under the influence of a strong adverse pressure gradient. Conversely, the slow decay of Eq. (5) with decreasing F/ν means that more eddy viscosity is generated near the solid surfaces, increasing the heat transfer and skin friction. This particular trend has some beneficial aspects, as the G–R variant will transition from laminar to turbulent flow without modification. As mentioned earlier, the Baldwin–Barth model requires the distance-dependent component of Eq. (6) to initiate the transition process.

Figure 4 compares the measured skin friction distribution at $X = 15.5$ cm with the computed distributions. The solutions

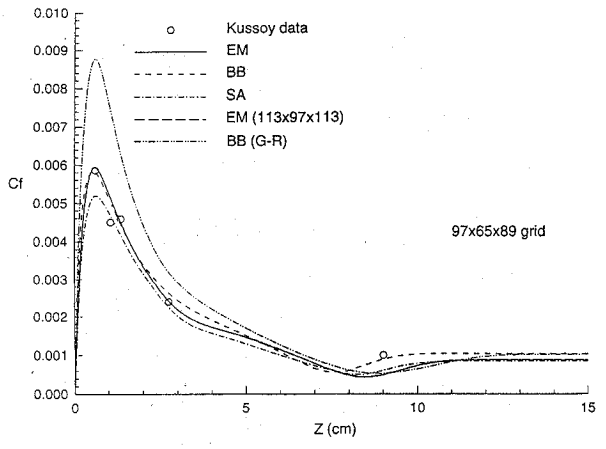

Fig. 4 Plate skin friction; Ref. 11 15-deg fin, $X = 15.5$ cm.

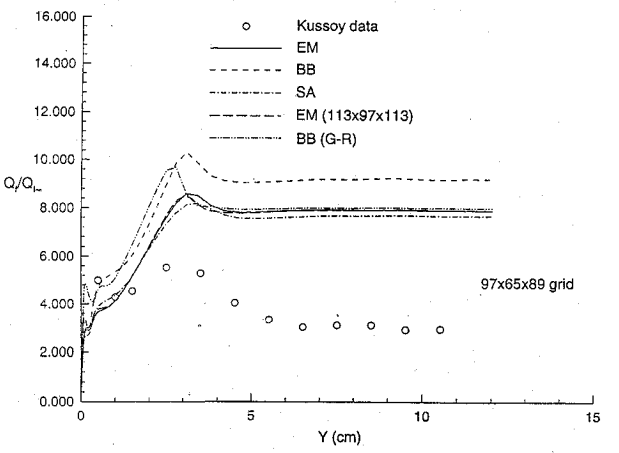

Fig. 6 Fin heat transfer; Ref. 11 15-deg fin, $X = 16.13$ cm.

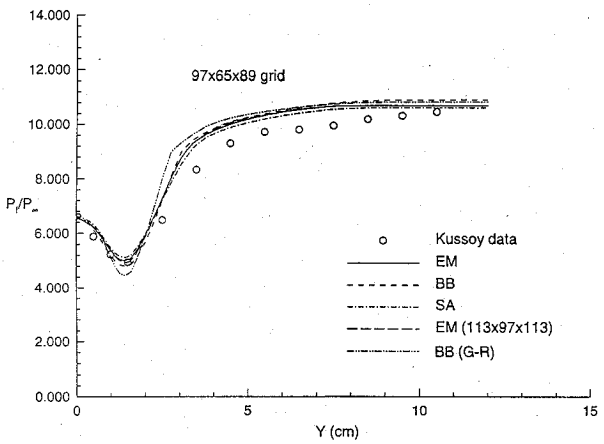

Fig. 5 Fin pressure; Ref. 11 15-deg fin, $X = 17.72$ cm.

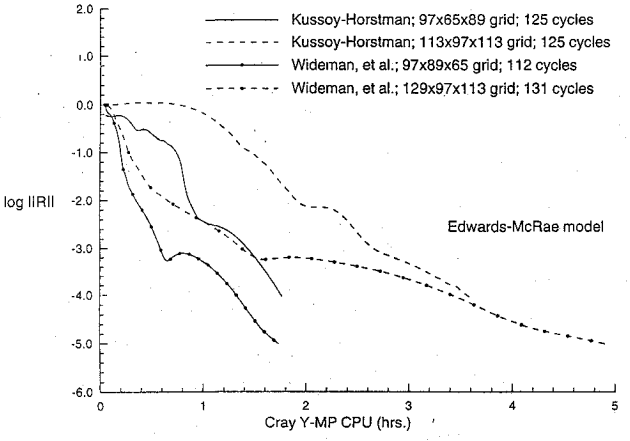

Fig. 7 Convergence histories; sharp fin and cylinder–cone interactions.

obtained using the Baldwin–Barth and Edwards–McRae models agree quite well with the rather sparse experimental data set, particularly near the fin. The Spalart–Allmaras result underpredicts the peak skin friction level, whereas the G–R solution overpredicts the peak level. The consistency of this behavior with that evidenced in Fig. 3 indicates that the computed flow in the corner region behaves in accordance with the Reynolds analogy created by the combination of the Boussinesq hypothesis and the constant turbulence Prandtl number assumption.

The surface pressure distribution along the fin at $X = 17.72$ cm is illustrated in Fig. 5. Generally good agreement with the experimental data is evidenced for all of the computations. Figure 6 compares the computed heat transfer distributions along the fin surface with the experimental data measured at $X = 16.13$ cm. The experimental distribution indicates that the fin boundary layer is laminar at the measurement station, except for a region near the plate surface ($Y = 0.0$ cm). None of the eddy viscosity–transport approaches predicts a purely laminar boundary layer on the fin. As shown in Ref. 15, however, this inaccuracy does not influence the surface properties along the plate to any large extent. Among the closure options, the Baldwin–Barth variants appear to produce the most abrupt transition, whereas the Edwards–McRae and Spalart–Allmaras models produce a more delayed response. As pointed out in Ref. 6, a lowering of the constant β in the damping function argument (6) can significantly affect the numerical transition distance predicted by the Edwards–McRae model. The value of this constant, 0.005, was chosen to ensure that the experimentally determined inflow boundary-layer properties were matched at the proper distance from the flat-plate leading edge (187 cm). This value was left unchanged for the actual interaction computation, leading to the results shown in Fig. 6.

As shown in Figs. 2–6, the effects of a twofold increase in grid resolution on the solution obtained using the Edwards–McRae model are minimal. Similar trends would probably hold for the other turbulence models. Figure 7 compares the convergence histories of the Edwards–McRae computation using both the $97 \times 89 \times 65$ and the $113 \times 97 \times 113$ grids. As indicated, the multigrid iteration strategy results in grid-independent convergence behavior to four decimal places in the residual norm, measured relative to its initial value. The convergence rates for the other turbulence models on the coarser grid (not shown) follow a very similar pattern. Higher levels of residual reduction could be achieved without difficulty; however, changes in the outputted surface quantities were negligible past the four order-of-magnitude reduction point.

Trends similar to those evidenced in Figs. 1–6 were also observed by Knight et al.,[15] who employed the Jones–Launder k–ϵ model and a two-layer k–ϵ/k–L model in their Navier–Stokes simulations. Given the differences in the level of mesh resolution and in the turbulence models, the agreement between the computed results of Ref. 15 and those of the present investigation is rather remarkable. In particular, the earlier simulations also overpredict the peak surface heat transfer level while accurately predicting the peak level of skin friction. Eliminating, for the time being, the possible need for an explicit compressibility correction in all models and the possibility of significant experimental error, it would appear that the major source of the disagreement between theory and experiment for this flow lies neither in the choice of turbulence model nor in the grid resolution but in the accuracy of the basic Boussinesq relation in the corner region.

B. Wideman et al. Cylinder–Cone

The second database utilized in the evaluation of the eddy viscosity–transport closures corresponds to a recent experiment of Wideman et al.[12] The basic geometry consists of a blended cylinder–20-deg cone combination in which the centerline of the cone is displaced from that of the initial cylinder section by a distance of 1.27 cm (half of the radius of the initial cylinder section). An X–R–θ coordinate system is used to facilitate the presentation of

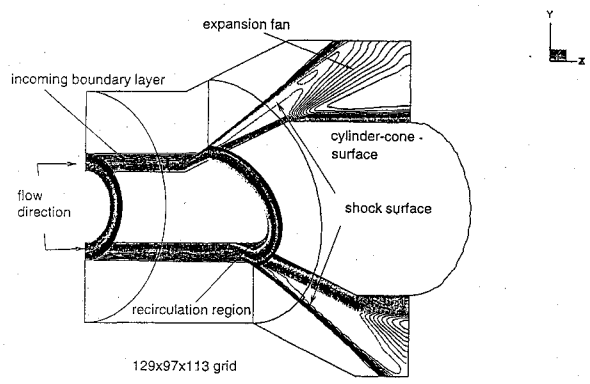

Fig. 8 Mach number contours; Ref. 12 20-deg cylinder–cone.

the computational and experimental results. The top and bottom of the cylinder are associated with $\theta = 0$ deg and $\theta = 180$ deg, respectively, whereas the origin of the axial coordinate X is located at the innermost $\theta = 0$ deg cylinder–cone juncture. Relative to this point, the axial displacement of the innermost juncture line is defined by

$$X = \frac{\hat{R}(\sqrt{5 - 4\cos\theta} - 1)}{2\tan 20} \tag{14}$$

where $\hat{R}$ is the radius of the initial cylinder section (2.54 cm). Another juncture line, displaced 10.47 cm downstream of the innermost juncture, defines the intersection of the cone with a larger cylinder (6.35 cm radius). A basic outline of the geometry is given in Fig. 8; Ref. 12 should, however, be consulted for further details.

Two grids, one with $97 \times 89 \times 65$ points in the X, R, and θ directions, and the other with $129 \times 97 \times 113$ points, are utilized in this study. The minimum radial grid spacing for both grids is 1.37×10^{-6} m, fine enough to ensure an inflow $\hat{n}^+_{\min}$ of less than unity. Points are also clustered in the vicinity of the innermost cylinder–cone juncture to resolve elements of the flow topology.

Mach number contours in the $\theta = 0$ deg and $\theta = 180$ deg symmetry planes and at two streamwise stations are shown in Fig. 8 ($129 \times 97 \times 113$ grid, Edwards–McRae model). The dominant inviscid features of the interaction are the oblique shock surface and the expansion fan formed due to the abrupt changes in the slope of the geometry aft of the innermost and outermost juncture lines. Because of the asymmetry of the configuration, the shock compresses the flow first at the top ($\theta = 0$ deg), inducing a pressure gradient in the circumferential direction. The nonuniform pressure distribution results in a general movement of the flow behind the shock surface from $\theta = 0$ to 180 deg. Associated with the development of the velocity component in the circumferential direction is the formation of a vortical structure that is roughly aligned with the innermost cylinder–cone juncture. Because of the lateral symmetry of the flow at $\theta = 180$ deg, the azimuthal movement of the flow is retarded, leading to a thickening of the boundary layer on the bottom of the configuration and the formation of a region of axially separated flow upstream of the cylinder–cone juncture.

Computed surface pressure distributions at five azimuthal stations, $\theta = 0, 45, 90, 135$, and 180 deg, are compared with the measured data in Fig. 9. The Baldwin–Barth, Edwards–McRae, and Spalart–Allmaras computations accurately predict both the general shape of the pressure distribution in the compression region and the upstream extent of the separation-shock pressure rise. The G–R computation overpredicts the extent of axial separation, particularly near the bottom of the cylinder–cone geometry. Near the rearmost cylinder–cone juncture, all solutions underpredict slightly the measured pressure level, an effect possibly attributable to insufficient streamwise grid resolution. At all azimuthal stations, the pressure distributions provided by the Edwards–McRae and Spalart–Allmaras models essentially collapse upon one another, providing another indication of the inherent similarity of the approaches in terms of predictive capability. The Baldwin–Barth solution underpredicts slightly the rate of pressure recovery downstream of the initial rise. The effect of grid refinement on the Edwards–McRae solution is to increase slightly the predicted level of upstream influence

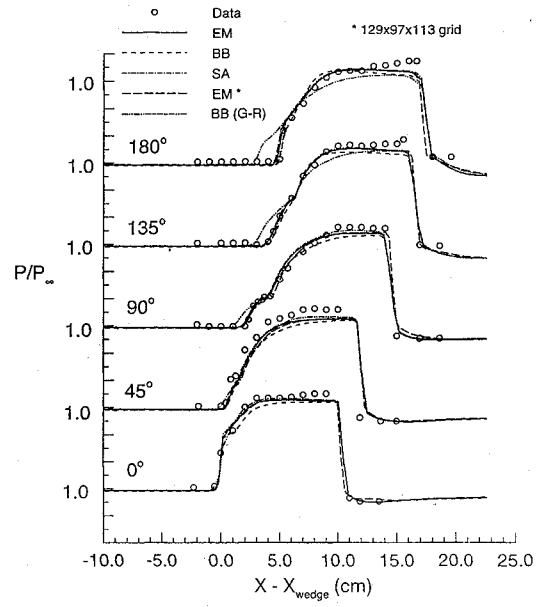

Fig. 9 Azimuthal surface pressure; Ref. 12 20-deg cylinder–cone: Edwards–McRae EM, Baldwin–Barth BB, Spalart–Allmaras SA, and Goldberg–Ramakrishnan BB (G–R).

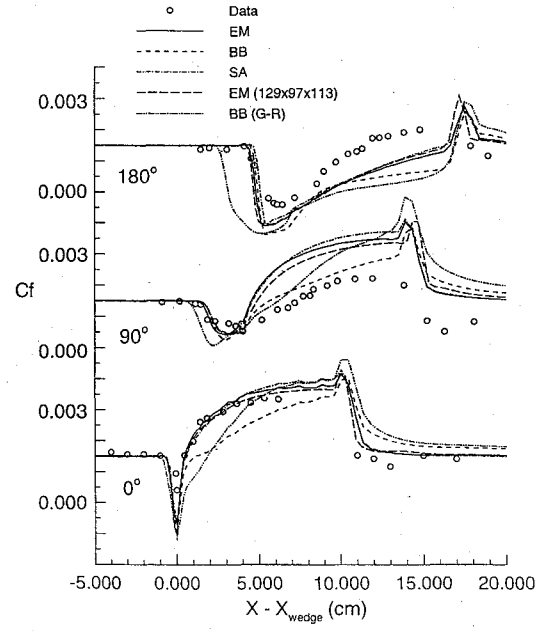

Fig. 10 Azimuthal skin friction; Ref. 12 20-deg cylinder–cone.

at $\theta = 180$ deg and to sharpen the pressure decrease in the vicinity of the outermost juncture line.

As in the Kussoy–Horstman configuration, more substantial differences among the model predictions occur with regard to the skin friction distributions (Fig. 10). At $\theta = 0$ deg, the Edwards–McRae and Spalart–Allmaras solutions accurately predict both the initial decrease in skin friction at the shock impingement location and its subsequent recovery downstream of the reattachment location. In contrast with two-dimensional results presented previously,[6] the rapid recovery of the near-wall velocity is due not only to an amplification in the turbulent fluctuation intensity caused by the shock wave but also to a general thinning of the boundary layer caused by the azimuthal movement of the flow. The Baldwin–Barth solution underpredicts significantly the rate of skin friction recovery downstream of reattachment, a trend very consistent with the results of Ref. 6. The G–R solution initially displays a delayed skin friction recovery but eventually asymptotes to the experimentally determined value. Again, this behavior is most likely due to the rather unusual behavior of the damping function of Eq. (5).

At $\theta = 90$ deg, significant near-wall velocity components in both the axial and circumferential directions are present. As before, the Baldwin–Barth, Edwards–McRae, and Spalart–Allmaras computations accurately predict the initial decrease in skin friction that delineates the forward extent of the crossflow vortical structure, whereas the G–R computation predicts a larger extent of crossflow separation. All solutions display a more rapid recovery of the streamwise component of the skin friction than is observed experimentally. In contrast with the results at $\theta = 0$ deg, the Baldwin–Barth model provides the more accurate prediction of the rate of skin friction recovery. The Spalart–Allmaras and Edwards–McRae computations overestimate the recovery rate significantly, whereas the G–R prediction is somewhere in between. It is possible that the reasonable agreement evidenced by the Baldwin–Barth model is fortuitous, given its failure to induce a proper recovery in other situations. It is also plausible, however, that the more coordinate-invariant nature of the model may permit a more accurate response to strong gradients in more than one direction.

At $\theta = 180$ deg, the Baldwin–Barth, Edwards–McRae, and Spalart–Allmaras computations predict the location of the separation point accurately but produce a stronger separation (indicated by a larger magnitude of skin friction coefficient) than is observed experimentally. The latter trend may contribute to the observed overprediction of the reattachment distance and the underprediction of the rate of recovery of the velocity field downstream of reattachment. The Spalart–Allmaras and Edwards–McRae distributions are very similar, whereas the Baldwin–Barth distribution deviates the most from the experimental data in the postreattachment region. The G–R variant of the Baldwin–Barth model results in a larger extent of axial separation, an effect again due to the extremely slow return of the damping function f_μ toward unity away from the surface. The grid-refined Edwards–McRae solution provides a slightly better prediction of the skin friction level in the recovery regions at $\theta = 0$ and 90 deg. The key features of the flow topology (discussed next) are, however, unaffected by the increase in resolution.

Figure 11 compares simulated surface oil-flow patterns in the interaction region with the postulated topology of Ref. 12. Results from the G–R version of the Baldwin–Barth model are not shown.

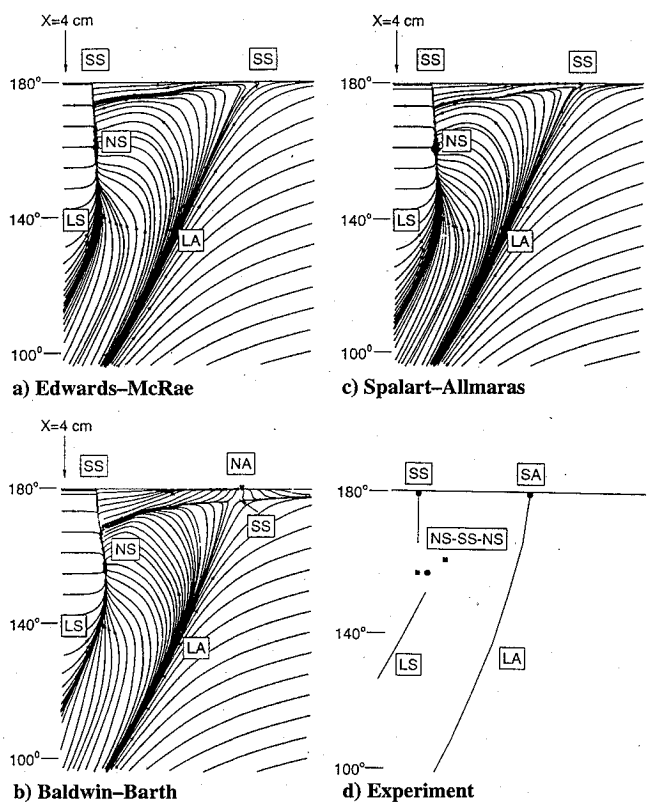

Fig. 11 Surface oil-flow patterns near $\theta = 180$ deg: line of attachment LA, node of attachment NA, saddle of separation SS, line of separation LS, node of separation NS, and saddle of attachment SA.

Except for anticipated differences in the positioning of certain features, the topological trends evidenced for the Baldwin–Barth model hold true for the G–R variant. For conciseness in presentation, the figure emphasizes the area near the $\theta = 180$ deg symmetry plane. The patterns were obtained by mapping the axial and circumferential components of velocity at the first grid station above the surface to the X–θ plane. Several singular (or critical) points, locations at which the surface shear stress vanishes and the local flow direction is nonunique, are clearly indicated in all of the computed patterns, as are lines of coalescence that demarcate the extent of the separation region. As shown in Ref. 16 among others, it is possible to determine directly the character of the singular points by applying a phase-space analysis to the surrounding flowfield. We postpone such a rigorous treatment until a later date and, instead, rely on the more phenomenological classification analysis of Chapman[17] to determine the nature of the computed singular points and their effect on the structure of the external flow.

One of the dominant features of the surface topology is a line of separation (LS) emanating from a saddle of separation at the top of the surface ($\theta = 0$ deg) and culminating at a node (focus) of separation (NS) located at $\theta \approx 160$ deg. The experimentally determined structure at $\theta \approx 160$ deg consists of two nodes (foci) of separation joined by a saddle of separation, a construct that will behave as a node of separation.[17] As a possible consequence of the relative simplicity of the closure assumptions, all of the computed solutions coalesce the node-saddle-node system into a single node. For all models, however, generally good agreement with the experiment is observed in the positioning of the topological features.

The line of separation marks the upstream extent of the vortical structure mentioned earlier; a line of attachment (LA) emanating from a node of attachment at $\theta = 0$ deg defines the downstream extent of the structure. Most of the fluid entrained into the crossflow vortex departs from the surface through the node of separation. A small portion of the near-wall fluid continues toward the $\theta = 180$ deg symmetry plane, where it moves upstream before departing from the surface at the forward saddle of separation (SS). A line of coalescence, located nearly parallel to the lower centerline, marks this division in the near wall flow and is present in all of the computed solutions. No such feature appears in the postulated topology of Ref. 12.

Near the $\theta = 180$ deg reattachment point, two distinct topological structures are present in the computed surface patterns, neither of which is completely consistent with the postulated experimental structure. In the Spalart–Allmaras and Edwards–McRae solutions, the rearmost line of attachment terminates in a saddle point located at the $\theta = 180$ deg centerline (Figs. 11a and 11c). As shown in Fig. 12a for the Edwards–McRae solution, the rearmost saddle point is nodelike in the $\theta = 180$ deg plane of symmetry, and the flow is away from the surface. According to Chapman,[17] such a topology implies that the rearmost critical point is a saddle of separation. Thus, on the lower surface, the Edwards–McRae and Spalart–Allmaras models both produce a saddle-of-separation to saddle-of-separation connection, a topology that is thought to be unstable except possibly under conditions of strong symmetry.[17] The flow pattern in the lower symmetry plane (Fig. 12a) indicates that the separation is open ended, as opposed to the closed-loop separation characteristic of a purely axisymmetric flowfield.

The surface topology predicted by the Baldwin–Barth computation near the $\theta = 180$ deg reattachment point is an example of a pitchfork bifurcation[17] caused, evidently, by differences in the eddy viscosity fields. Here, the saddle of separation predicted by the other simulations is replaced by a node of attachment and two new saddles of separation located on either side of the centerline. Because of symmetry, only one of the saddles is shown in Fig. 11b. Associated with the differences in type (attachment vs separation) among the critical points is an additional critical point located off the surface within the centerline plane (see Fig. 12b). Whereas the separation in the lower symmetry plane is obviously still open ended, the details of the near-wall flow structure are considerably more complex than those corresponding to the Edwards–McRae/Spalart–Allmaras topology and are the subject of current study.[18]

The authors of Ref. 12 maintain that the rearmost line of attachment culminates in a saddle point. They conclude, however, that the

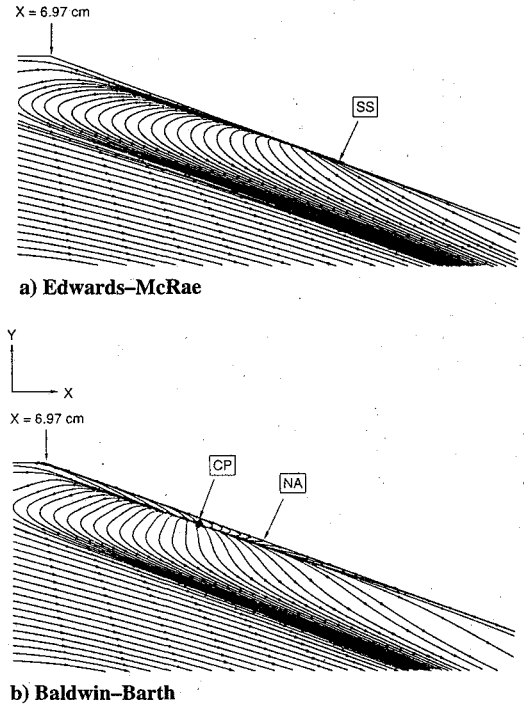

Fig. 12 Symmetry plane streamlines near reattachment, $\theta = 180$ deg: saddle of separation SS, critical point CP, and node of attachment NA.

rearmost saddle is one of attachment, a topology that would imply the existence of a closed-loop separation in the $\theta = 180$ deg symmetry plane. They also state, however, that their oil-flow resolution might not have been high enough to capture other critical points in the reattachment region and that their saddle-of-attachment conclusion was based heavily on the surface pattern.[12] Based on these comments and given the obvious weaknesses of all of the models in the prediction of the skin friction response in the reattachment/recovery region, it is not clear at this point which (if any) of the postulated topologies most closely represents the actual flowfield. If the saddle–saddle connection is accepted, however, the topology produced by the Edwards–McRae and Spalart–Allmaras models does provide a plausible alternative to the structure detailed in Ref. 12. Comparisons of the eddy viscosity–transport results with those of other turbulence closure options are currently under way.[18] The obtained results might clarify the situation, but only the availability of a more detailed experimental data set that includes velocity measurements in the lower symmetry plane will resolve the dilemma entirely.

Convergence histories corresponding to the Edwards–McRae simulations of the Wideman et al. flow are also illustrated in Fig. 7. As before, the upwind relaxation multigrid algorithm performs well, reducing the residual error on the coarser mesh by five orders of magnitude in 112 cycles. On the finer $129 \times 97 \times 113$ mesh, a similar level of reduction requires 131 cycles, indicating that grid-independent convergence rates are not quite achieved for this particular sequence of meshes.

V. Conclusions

This work completes an effort designed to test the performance of several one-equation eddy viscosity–transport turbulence models in computing strongly interacting compressible flows in two and three dimensions. Two recent experiments, one involving the Mach 8 interaction of a fin-generated oblique shock with a developing flat-plate boundary layer and the other involving Mach 3 flow over a cylinder–cone configuration, have been numerically simulated using a recently developed multigrid approach. Fine grids have been utilized throughout to reduce uncertainties associated with the discretization error.

The current results indicate that three of the tested one-equation models (Baldwin–Barth, Edwards–McRae, and Spalart–Allmaras) provide good agreement with the measured pressure distributions, particularly in the prediction of the upstream (or lateral) extent of the separated boundary layer. The pointwise Baldwin–Barth model of Goldberg and Ramakrishnan tends to overpredict the extent of separation, an effect due to the adverse influence of the wall-damping functions in regions away from the solid surfaces. After the completion of this study, the authors were informed that an alternative version of the Goldberg–Ramakrishnan model, incorporating a slightly different definition of f_μ, had been published.[19] Our preliminary investigations indicate that this newer version provides results very similar to that of the original Baldwin–Barth model. In concert with previous two-dimensional results, more significant deviations from the experimental data and from each other occur in the skin friction and heat transfer distributions. For the sharp fin interaction, all of the tested closures overpredict the peak heat transfer level near the fin–flat-plate juncture, a trend consistent with the results of other numerical simulations using different closure approaches and different levels of grid resolution.

For the cylinder–cone configuration, the Baldwin–Barth model induces a very poor rate of skin friction recovery in regions where the two-dimensional nature of the interaction is predominant but performs better than the other models in regions where both axial and circumferential components of the near-wall velocity are important. In regions where the flow is axially separated, all models produce a stronger separation than is observed experimentally. An associated effect is a rather poor prediction of the recovery rate of the velocity field downstream of the reattachment point. It is possible that alternative calibrations for the near-wall region, based on something other than the logarithmic law in adverse pressure gradient situations, may have to be considered in order to alleviate this difficulty.

A preliminary analysis of the structure of the cylinder–cone flow has also been performed. Most of the topological features present in the experimental surface oil-flow patterns are also found in the computed patterns, and good agreement in the positioning of the features is generally observed. Differences in interpretation make further study necessary before a complete understanding of the flow structure can be achieved; however, the obtained results do illustrate the importance of accurate flow topology prediction in the construction and validation of turbulence models for three-dimensional flowfields. It is of some interest that the Edwards–McRae and Spalart–Allmaras computations both predict a saddle-to-saddle connection on the bottom of the configuration, a feature that is in accord with the experimental results. The Baldwin–Barth model results in a pitchfork bifurcation of the rearmost saddle point into a node, two saddles offset from the centerline, and a critical point located above the surface.

It is apparent from the current results and from the results of earlier efforts that the tested eddy viscosity–transport closures offer a good level of accuracy and predictive capability for strongly compressible, shock-separated flows. The failure to induce the correct rate of boundary-layer recovery following an axial separation is a significant weakness of this class of models; however, the low cost and robustness of the eddy viscosity–transport formulations make them very attractive as replacements for algebraic models in production-level computational fluid dynamics codes.

Acknowledgments

This work was partially supported by the NASA Center of Research Excellence Program (NAGW-2924). Cray Y-MP computing time was provided courtesy of grants from the North Carolina Supercomputing Center and from NASA Lewis Research Center. The first author would like to thank J. L. Brown of NASA Ames Research Center for providing the data sets and other useful information regarding the cylinder–cone experiment.

References

[1]Nee, V. W., and Kovasznay, L. S. G., "Simple Phenomenological Theory of Turbulent Shear Flows," *Physics of Fluids*, Vol. 12, No. 3, 1969, pp. 473 and 484.

[2]Baldwin, B. S., and Barth, T. J., "A One-Equation Turbulence Transport Model for High Reynolds Number Wall-Bounded Flows," NASA TM-102847, Aug. 1990.

[3]Spalart, P. R., and Allmaras, S. R., "A One-Equation Turbulence Model for Aerodynamic Flows," AIAA Paper 92-0439, Jan. 1992.

[4]Durbin, P. A., and Yang, Z., "A Transport Equation for Eddy Viscosity," *Proceedings of the 1992 Summer Program*, Center for Turbulence Research, 1992, pp. 293–303.

[5]Edwards, J. R., and McRae, D. S., "Nonlinear Relaxation Navier–Stokes Solver for Three-Dimensional, High-Speed Internal Flows," *AIAA Journal*, Vol. 31, No. 7, 1993, pp. 1222–1228.

[6]Edwards, J. R., and Chandra, S., "Eddy Viscosity–Transport Turbulence Models for High-Speed, Two-Dimensional Shock-Separated Flowfields," AIAA Paper 94-0310, Jan. 1994.

[7]Menter, F. R., "Performance of Popular Turbulence Models for Attached and Separated Adverse Pressure Gradient Flows," *AIAA Journal*, Vol. 30, No. 8, 1992, pp. 2066–2072.

[8]Kandula, M., and Buning, P. G., "Evaluation of Baldwin–Barth Turbulence Model with an Axisymmetric Afterbody-Exhaust Jet Flowfield," *AIAA Journal*, Vol. 31, No. 9, 1993, pp. 1723–1725.

[9]Birch, S. F., "One Equation Models Revisited," AIAA Paper 93-2903, July 1993.

[10]Goldberg, U. C., and Ramakrishnan, S. V., "A Pointwise Version of the Baldwin–Barth Turbulence Model," AIAA Paper 93-3523, Aug. 1993.

[11]Kussoy, M. I., and Horstman, K. C., "Documentation of Two- and Three-Dimensional Shock-Wave/Turbulent Boundary-Layer Interaction Flows at Mach 8.18," NASA TM-103838, 1991.

[12]Wideman, J. K., Brown, J. L., Miles, J. B., and Ozcan, O., "Skin Friction Measurements in a 3-D, Supersonic Shock-Wave/Boundary Layer Interaction," AIAA Paper 94-0314, Jan. 1994.

[13]Wada, Y., and Liou, M. S., "A Flux-Splitting Scheme with High Resolution and Robustness for Discontinuities," AIAA Paper 94-0083, Jan. 1994.

[14]Edwards, J. R., "Development of an Upwind Relaxation Multigrid Method for Computing Three-Dimensional, Viscous Internal Flows," AIAA Paper 95-0208, Jan. 1995.

[15]Knight, D. K., Horstman, C. C., and Monson, D. J., "The Hypersonic Shock Wave/Turbulent Boundary Layer Interaction Generated by a Sharp Fin at Mach 8.2," AIAA Paper 92-0747, Jan. 1992.

[16]Perry, A., and Chong, M., "A Description of Eddying Motions and Flow Patterns using Critical Point Concepts," *Annual Review of Fluid Mechanics*, Vol. 19, 1987, pp. 125–155.

[17]Chapman, G. T., "Topological Classification of Flow Separation on Three-Dimensional Bodies," AIAA Paper 86-0485, Jan. 1986.

[18]Gaitonde, D., Edwards, J. R., and Shang, J. S., "The Computed Structure of a 3-D Turbulent Interaction Caused by a Cylinder/Offset-Flare Juncture," AIAA Paper 95-0230, Jan. 1995.

[19]Goldberg, U. C., and Ramakrishnan, S. V., "A Pointwise Version of the Baldwin–Barth Turbulence Model," *Computational Fluid Dynamics*, Vol. 1, 1993, pp. 321–338.